

An Empirical Model for Multiple-Scattered Radiation in FUV

Nimmi Narayanan^{1,2} and N. V. Sujatha¹ Department of Physics, St. Xavier's College for Women, Aluva, Kerala 683101, India

Sree Sankara College, Kalady, Kerala 683574, India

Received 2025 January 27; revised 2025 July 22; accepted 2025 September 10; published 2025 October 15

Abstract

In this work, we present a systematic comparison of single- and multiple-scattering models for dust-scattered starlight across the UV sky and attempt to derive a simulation model of multiple-scattered radiation using the single-scattered radiation. Our new simulated multiple-scattering model uses a critical angle (θ_c), which is dependent on optical depth (τ), albedo (a), and phase function asymmetry (g), to replace the computationally intensive full Monte Carlo treatment. We find that multiple-scattering becomes increasingly important in almost all optical depths, depending on the scattering geometry. UV-bright stars show a peak scattering intensity near the stellar disk, dropping by an order of magnitude within $10^{\circ}-15^{\circ}$ and merging with the background at $40^{\circ}-50^{\circ}$, whereas fainter or more distant stars require larger angular separations to reach the same relative reduction. We introduce a functional form, $I_{\theta} = I_0(1 - \tanh(SP \times \theta))$, to describe the radial decrease in scattered intensity, with the slope parameter declining systematically for more distant stars. Depending on a star's position, multiple-scattered fluxes can exceed single-scattered fluxes by up to 200%, and both converge at a critical angle, θ_c , which depends logarithmically on stellar distance and is governed by τ , a, and g. Notably, θ_c remains independent of Galactic longitude or latitude, underscoring the robust, geometry-driven nature of the scattering process.

Key words: methods: data analysis - stars: distances - (ISM:) dust, extinction - ultraviolet: ISM

1. Introduction

Interstellar dust constitutes a minor fraction of the interstellar medium, yet is crucial in the evolutionary processes of stars and galaxies (Savage & Mathis 1979). Dust scattering and absorption mechanisms significantly contribute to the extinction of the Interstellar Radiation Field (ISRF; Trumpler 1930). Dust scattering predominantly occurs at shorter wavelengths ranging from 10 to 400 nm (Draine 2003), while absorption of high-energy radiations results in thermal emission in the low-energy spectrum, especially in the infrared at $100 \, \mu \text{m}$ (Bernstein et al. 2002). Systematic analysis and modeling of these phenomena reveal the actual dust distribution and its optical properties along the line of sight (Draine 2003).

Diffuse radiation in the sky spans the entire electromagnetic spectrum, from radio to gamma rays. Among these, the ultraviolet (UV) region is significant for dust scattering studies, as a limited number of UV-bright stars play an important role in diffuse radiation, helping to detect weak diffuse radiation (Henry 1991; Gordon 2004). Typically, a single-scattering model in low-density regions and a Monte Carlo multiple-scattering model in high-density regions are used to estimate the dust-scattered radiation. Studies indicate that at lower optical depths, where scattering remains minimal, the single- and multiple-scattering intensities converge to nearly the same values (Murthy & Henry 1995; Henry et al. 2014). Multiple-

scattered (MS) radiation has also been observed to be 30% greater than single-scattered (SS) radiation, even in the absence of reddening (Murthy 2016). However, factors influencing dust-scattering encompass stellar distribution, dust composition, distribution, and the scattering function.

The Henyey–Greenstein (HG) scattering function, commonly used in these studies, is a mathematical model that simulates light scattering in dusty environments, such as interstellar space, by providing the angular distribution of photon scattering caused by interstellar dust or particles (Henyey & Greenstein 1941). The optical parameters albedo (a) and the phase function asymmetry factor (g) depend on the dust grain size, shape, and composition and are crucial for understanding the dust properties (Draine 2003). A realistic radiative transfer model is nonlinear, non-local, and multi-wavelength in nature and the detailed procedure is discussed in Steinacker et al. (2013). A Monte Carlo Radiative Transfer (MCRT) approach is necessary for analyzing dust scattering in denser regions, such as reflection nebulae, dark clouds, and low-latitude diffuse galactic light, as it provides deeper insights into dust optical parameters (Gordon 2004).

In this work, we estimate the dust-scattered starlight at farultraviolet (FUV) using both multiple- and single-scattering models from the same stellar and dust environments and compare the emissions by varying the dust parameters and stellar angular separation from the line of sight along the latitude and longitude directions. We aim to establish a relationship between multiple- and SS intensities through a comparative analysis of model outputs, especially for optical depths, $\tau \leqslant 1$. Further, we validate the relation using the observed diffuse FUV radiation from Galaxy Evolution Explorer (GALEX) deep observations toward the CDFS region at 1550 Å located near the south galactic pole and Voyager observations toward Ophiuchus region at 1100 Å. This relation can facilitate the prediction of dust-scattered radiation from optically dense regions without relying on the time-consuming multiple-scattering model.

2. Observations

In 2003, NASA launched the GALEX space telescope to study the universe in UV radiation. Operating across two UV bands, FUV at 135–175 nm and near-ultraviolet (NUV) at 175–280 nm, GALEX captured fine details of UV emissions for a decade that are otherwise invisible, with a spatial precision of 5" using a high-sensitivity microchannel plate detector (Martin et al. 2005; Morrissey et al. 2007). Through wide-field surveys and deep observations, GALEX gathered comprehensive UV data, which have been instrumental in refining models of star formation rates, galaxy morphology, large-scale structure of the cosmos, and dust scattering.

Using the archival data from the GALEX mission, Murthy et al. (2010) mapped the diffuse UV cosmic background in two wavelength bands (FUV: 153 nm; NUV: 231 nm) across nearly 75% of the sky, uncovered areas of active star formation, and traced large-scale features in the universe. GALEX observations and discoveries have significantly improved our understanding of the diffuse UV sky and laid the groundwork for astrophysical studies on cosmic background emissions and their components.

The Ultraviolet Spectrometers (UVS) aboard Voyager 1 and 2 measured diffuse UV background radiation from 50 to 170 nm, with maximal sensitivity below 120 nm. At great heliocentric distances, these sensors provide a rare, uncontaminated view of the UV sky, which helps discover spatial fluctuations and distinguish Galactic from extragalactic components. With a spectral resolution of \sim 38 Å and a field of view of 0.1×0.87 , Voyager UVS can detect diffuse radiation with a sensitivity of over 100 photon units. In addition to planetary observations, the spacecraft has scanned numerous astronomical locations to constrain the UV background contributions of interstellar dust scattering and presumed cosmological sources. We validated our simulated multiple-scattering model using 10 GALEX targets toward the CDFS region and six Voyager targets in and around the Ophiuchus molecular cloud at 1100 Å from low optical depth regions.

3. Scattering Models

Stellar radiative transfer involves stellar photons interacting with intergalactic or interstellar dust and gas and can scatter, absorb, or radiate. The radiation field at any location is crucial in the simulation of dust grain scattering and absorption. The ISRF model of Sujatha et al. (2004) can predict the ISRF at any point in the sky within a few hundred parsecs of the Sun. The ISRF in the UV is largely caused by hot early-type stars that generate UV radiation. The ISRF Model utilizes the Hipparcos star catalogue, which provides accurate stellar distances for 107,514 stars of spectral class earlier than R, of which only 10%-15% contribute in the UV (Sujatha et al. 2004). The intrinsic luminosity of each star in the model was determined using the Kurucz Model (Kurucz 1992) and scaled to its visual magnitude to calculate its stellar luminosity. Any scattering model depends on scatterers' position, density, dust grain properties, and sources' position and fluxes. Energetic photons scatter many times before reaching the detector. Since radiative transfer equations are complicated and geometrydependent, especially in high optical depth regions, we have to use the Monte Carlo approach to simulate this process.

We individually analyzed the variation of dust-scattered starlight from selected bright stars in the Hipparcos star catalogue (Perryman et al. 1997) at a fixed line of sight, employing a singlescattering model with a specified dust distribution. In our model, we have considered a dust distribution corresponding to an optical depth of 0.5 in such a way that a neutral hydrogen column density of $N_{\rm H} = 3.27 \times 10^{20} \, \rm cm^{-2}$ distributed at 110 pc represents a farther cloud, after accounting for the local fluff distribution of $4.94 \times 10^{18} \, \mathrm{cm}^{-2}$ up to 20 pc and $3.2 \times 10^{19} \, \mathrm{cm}^{-2}$ at 60 pc as a nearer cloud (Corradi et al. 2004). More details about the model are described in Sujatha et al. (2005, 2007). By varying the stellar angular separation by 2° from the line of sight in both longitude and latitude directions, we observed that the scattered intensity of most contributing stars diminishes to one-tenth of the maximum value within an angular distance of $\leq 10^{\circ}$ (Figure 1). We also found that the stellar angular distance associated with a one-tenth reduction in scattered intensity increases as the scattering contribution of a star decreases, either because of its distance or its brightness. This is apparent from the percentage variation of the scattered intensity plots against stellar angular separation in both longitudinal and latitudinal directions (Figure 2).

Murthy (2016) implemented a Monte Carlo model that uses a mixture of graphite and silicate grains with an R_V of 3.1 and a mean ratio of total neutral hydrogen to color excess, $\frac{N(H)}{E(B-V)}$ of $5.8 \times 10^{21} \, \mathrm{cm}^{-2} \, \mathrm{mag}^{-1}$ (Bohlin et al. 1978), to estimate the dust-scattered starlight across our Galaxy. In this work, we employed an identical Monte Carlo methodology referenced in Murthy (2016), Sujatha et al. (2007), utilizing Hipparcos stars and their flux (Sujatha et al. 2004), as the photon source. Here, each stellar photon is presumed to be emitted in a random direction and to propagate in a linear trajectory until it encounters interstellar dust grains. The probability of photon contact depends upon the dust grains' local density and cross-section, as derived from the Milky Way model (Weingartner & Draine 2001; Draine 2003). Following each encounter, the

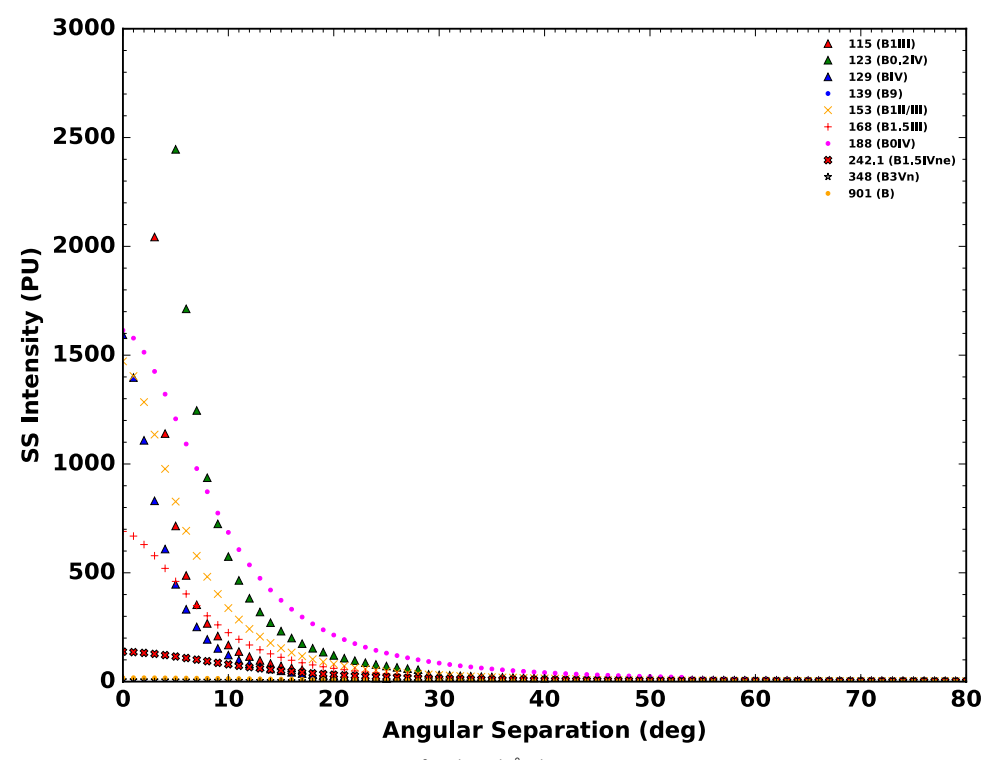


Figure 1. Variation of the SS intensity in PU (1 PU = 1 photons cm⁻² s⁻¹ sr⁻¹ \mathring{A}^{-1}) of various stars with stellar angular separation in the longitude direction.

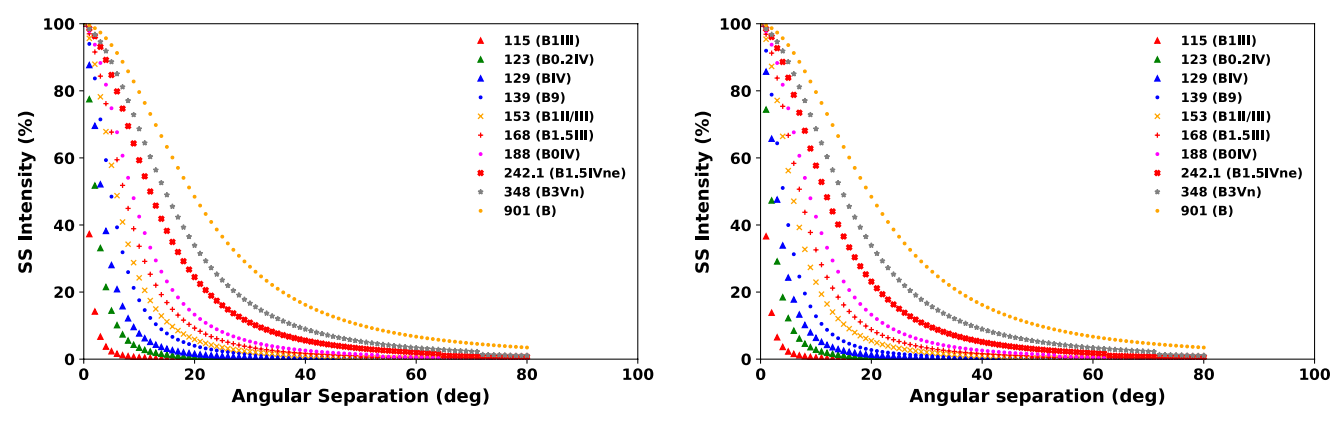


Figure 2. Percentage variation of SS intensity of various stars with stellar angular separation along Galactic latitude (left) and longitude (right).

photon weight diminishes by the albedo and is redirected with a probability derived from the HG scattering function (Henyey & Greenstein 1941)

$$\phi(\theta) = \frac{1}{4\pi} \frac{(1 - g^2)}{(1 + g^2 - 2g\cos(\theta))^{1.5}},\tag{1}$$

where g is the phase function asymmetry factor $(g = \langle \cos \theta \rangle)$ and θ is the scattering angle. Each photon is tracked until its energy becomes negligible or it leaves the dust grid area. The program executes for 10^7 weighted photons emitted from each star for each value of a and g.

4. An Empirical Model for Multiple Scattering

We have plotted the SS intensity at 155 nm for 10 stars from different locations as a function of stellar angular separation from the line of sight in Figure 1. The figure illustrates how SS light from hot, early type-B stars reaches a strong peak close to the stellar disk and then drops sharply within the first 10° – 15° of angular separation from the line of sight. Differences in the maximum brightness can be attributed to the intrinsic stellar brightness, spectral type, luminosity class-dependent dust scattering efficiency, and the distance of the scattering material. By roughly 20° – 30° of angular separation, the

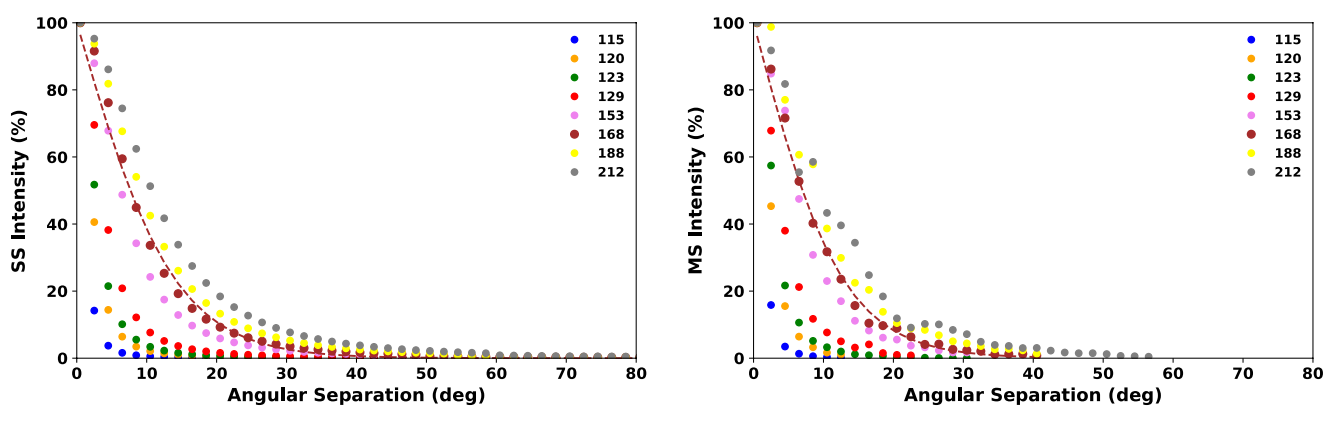


Figure 3. Percentage variation of single (left) and multiple-scattered intensities (right) plotted against the stellar angular separation. The SP of the hyperbolic curve decreases as the stellar distance increases.

Table 1
Details of Hipparcos Stars Used in the Study

HD No	gl (deg)	gb (deg)	Distance (pc)	Spectral Type	Stellar Flux at 1550 Å (erg cm ⁻² s ⁻¹ Å ⁻¹)
118716	310.19	8.72	115.21	B1III	1.33E-08
9531	132.32	-24.85	120.19	B9IV	5.87E-11
143275	350.10	22.49	123.15	B0.2IV	2.92E-08
144470	352.75	22.77	129.87	B1V	5.40E-09
44743	226.06	-14.27	153.14	B1II/III	1.62E-08
129056	321.61	11.44	168.07	B1.5III	1.13E-08
5394	123.58	-2.15	187.97	B0IV:evar	3.75E-08
45725	216.66	-8.21	211.86	B3Ve	2.54E-09

intensities typically fall to only a small fraction of their peak levels, in line with known scattering phase functions. Beyond $40^{\circ}-50^{\circ}$, the measured fluxes for all stars approach the background limit. The overall height of each curve is governed by a combination of stellar luminosity, spectral energy distribution, and the local dust column as well as the geometry of the scattering environment. These findings are also reflected in Figure 2 which shows that the scattered flux primarily depends on the star's spectral type and its angular separation from the scattering point, with latitude and longitude having minimal influence. As the separation increases, SS light from hot, early-type stars drops rapidly from near 100% at zero degrees to below 10% by $10^{\circ}-15^{\circ}$, and only a few percent by 20° . This pattern remains consistent across both Galactic latitude and longitude.

Using both the single and multiple-scattering models, the dust-scattered starlight was estimated for a subset of the brightest stars considered earlier, whose details are provided in Table 1. Here, we excluded distant stars beyond 300 pc as their contribution is minimal (see Figure 1) relative to the selected stars. The percentage variation of scattered intensities obtained

from both models is plotted against stellar angular separation in Figure 3. A hyperbolic tangent relation with a specific slope parameter (SP) for each star characterizes the variation in scattered flux of each star with its angular separation from the line of sight. Hence, the variation in the scattered intensity of a star, as a function of angular separation, can be mathematically expressed in terms of the SP and the angular distance, θ , of the star from the scattering location as

$$I_{\theta} = I_0(1 - \tanh(SP \times \theta)), \tag{2}$$

where I_0 and I_θ represent the scattered intensity measured at angular separations of 0.5 and θ° from the line of sight, respectively.

$$SP = 1.3 (d)^{-0.7}. (3)$$

Figure 4 shows that the SP declines monotonically with increasing stellar distance, d (in parsec), from the scattering region, following a power-law given in Equation (3). Both single-scattering (red and blue bullets) and multiple-scattering (red and blue stars) points track this best-fit curve closely, indicating that the hyperbolic dependence on distance is robust. Moreover, there is no major systematic offset between the latitude (red) and longitude (blue) directions, suggesting that scattering geometry is broadly consistent in both orientations. The model outputs for each star with an albedo a = 0.4 and g = 0.6 are utilized to analyze the variations in the ratio of multiple- to SS intensities as a function of the angular separation from the line of sight (Figure 5). The ratio is highest at small angular separations and decreases with increasing separation, suggesting that multiple-scattering is most significant near the star's line of sight. Despite minor variations across different stellar distances, the overall behavior is consistent in both latitude and longitude directions. The results establish that an increase in angular separation corresponds to a nonlinear decrease in the ratio, which can be expressed

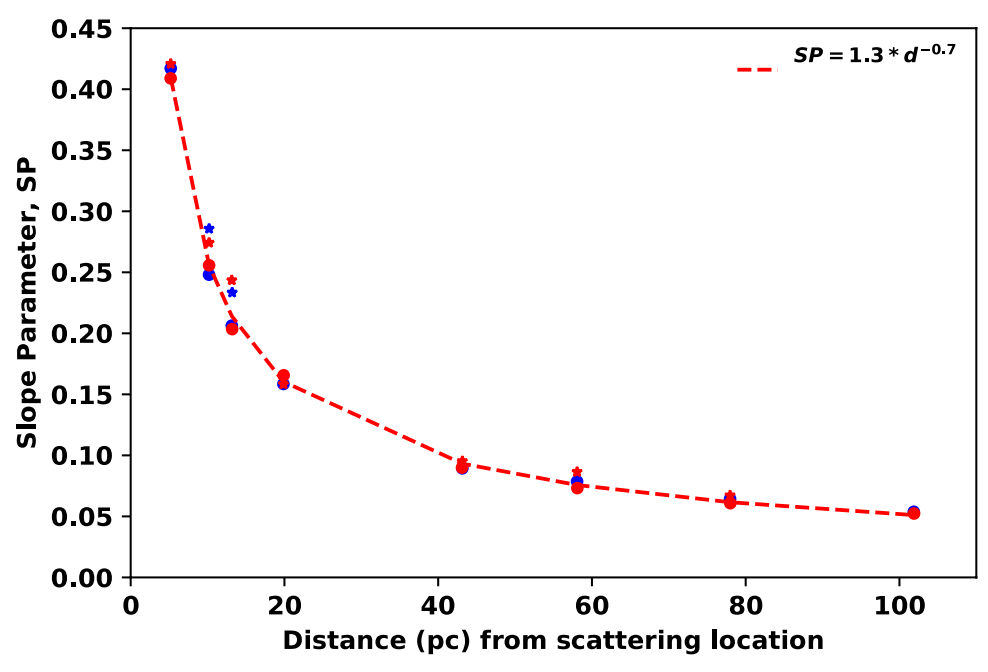


Figure 4. Hyperbolic SPs obtained from scattering models (SS: "bullets" and MS: "stars") are plotted against stellar distance from scattering location toward latitude (red) and longitude (blue) directions. The dashed line represents the best-fit curve and shows the relation between them.

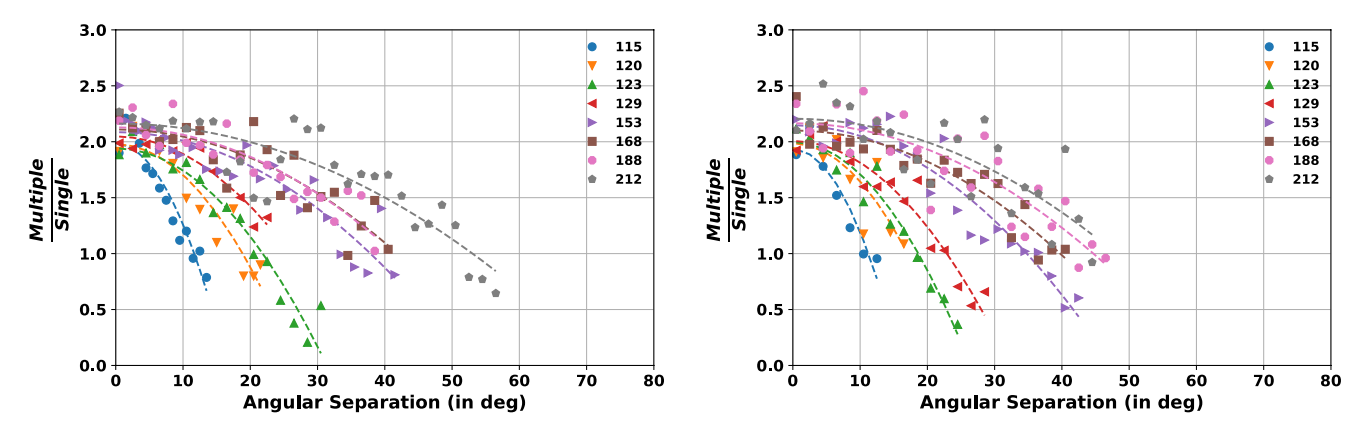


Figure 5. Ratio between multiple and single-scattering intensity for an (a, g) combination of (0.4, 0.6) is plotted against the stellar angular separation from the line of sight toward latitude (left) and longitude (right) directions.

mathematically as follows

$$\frac{I_{\rm MS}}{I_{\rm SS}} = 2 - \left(\frac{\theta}{\theta_c}\right)^2,\tag{4}$$

where θ denotes the angular separation of the star from the line of sight, while θ_c indicates the critical angle where multiple-scattered flux equals the SS flux. The schematic representation of these parameters is depicted in Figure 6. Figure 7 shows that the critical angle, θ_c , increases with the star's distance from the scattering site, following a logarithmic trend for both Galactic latitude and longitude (see Equation (5)). θ_c rises from about 10° at small distances (≤ 10 pc) to nearly 50° at larger distances (~ 100 pc), suggesting that more distant stars require

a wider angular separation before multiple-scattering effects match single-scattering intensities.

$$\theta_c = 13 \log (SF * d), \tag{5}$$

where d represents the stellar distance in pc from the scattering location and the slope factor (SF) is a function of optical depth and optical constants. The above exercise was repeated by varying the optical depth, τ , albedo, a, and phase function asymmetry factor, g, revealing that the critical angle θ_c increases with distance from the scattering location, but is also controlled by these parameters. A higher τ lowers θ_c , indicating the significant influence of multiple scattering in optically dense regions. In contrast, increasing a or g shifts θ_c

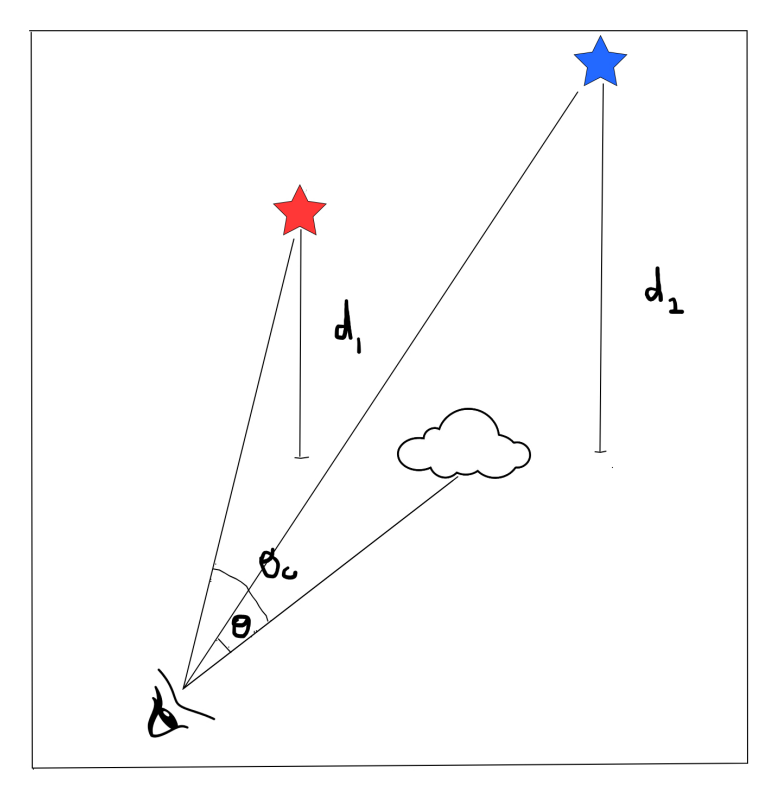


Figure 6. Schematic representation of scattering parameters - angular (θ) and critical angle (θ_c) separation from line of sight and distance from the scattering location (d).

to larger values, reflecting enhanced forward scattering efficiency. Meanwhile, the SF linearly depends on these optical parameters. The changes in the critical angle with optical depth ($\tau \leq 1$) and optical constants are shown in Figure 8, while changes in the SF are illustrated in Figure 9. Considering these facts, Equation (5) can be generalized to accommodate the combined effects as follows

$$\theta_c = 13 \log ([(-0.78\tau + 0.87) + (0.54a + 0.33) + (0.15g + 0.38)]d/3), \tag{6}$$

$$\theta_c = 13 \log ([0.18a + 0.05g - 0.26\tau + 0.53]d),$$
 (7)

where τ , a, g and d are the optical depth, albedo, phase asymmetry factor and stellar distance (in parsec) from the scattering location respectively.

5. Validation of the Empirical Model

For validation, 10 GALEX deep observations toward a low-dense region (CDFS) were selected from the GALEX-MAST archive. The observation log and the details of foreground contamination in each observation (Narayanan et al. 2023) are tabulated in Table 2. Following Sujatha et al. (2009, 2010), we extracted the total sky background for each observation, which included foreground emissions (instrumental dark count, airglow, and zodiacal light) and astrophysical signals (atomic and molecular emissions, dust-scattered starlight, extragalactic

contributions, etc.), by eliminating point sources from the merged GALEX point-source catalog and binning the observations into 2' pixels (80×80 GALEX pixels) to enhance the signal-to-noise ratio. The diffuse FUV background was extracted by subtracting the foreground contamination from each field as assessed by Narayanan et al. (2023).

We have analyzed the dust-scattered starlight in the CDFS region using our single- and multiple-scattering models by positioning the scattering cloud at 120 pc in addition to the distribution of local fluff as discussed earlier. We have seen that 24 stars listed in Table 3 account for approximately 50% of the ISRF along the line of sight. Therefore, due to the impracticality of executing MCRT code for all Hipparcos stars, the multiplescattering model runs for these stars and the resulting flux were combined with the SS fluxes of the remaining stars in each case. By comparing the observed FUV sky background, the singlescattering model achieves its best-fit ($\chi^2_{\rm min}=0.69$) at a=0.6and g = 0.65. In contrast, the multiple-scattering model yields a $\chi^2_{\rm min} = 1.3$, with corresponding 1σ confidence intervals of $a = (0.47 \pm 0.07)$ and $g = (0.62 \pm 0.07)$ (Figure 10). The empirical SMS model (Equations (4) and (7)) identifies optimal parameters of a = 0.5 and g = 0.7. Figure 11 compares the SS (blue stars), MS (black stars), and SMS (red stars) model outputs at their respective minimum χ^2 against the observed diffuse background radiation.

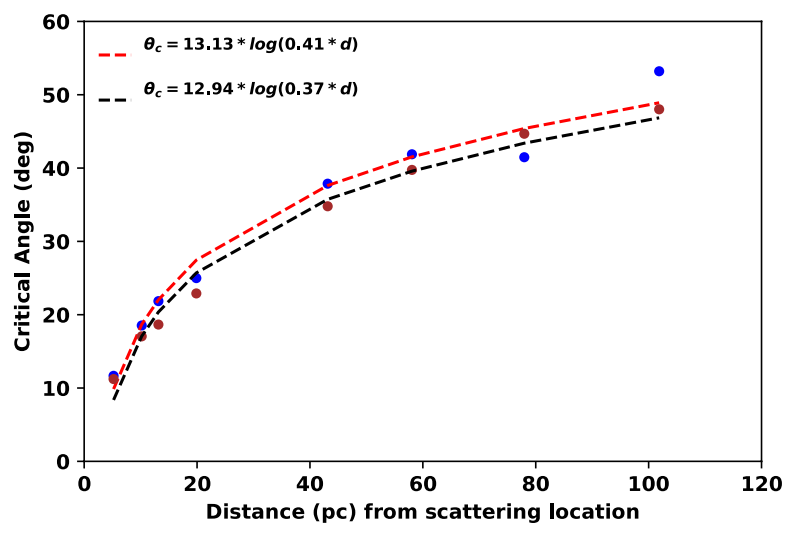


Figure 7. The critical angular separation (θ_c) plotted for different stars as a function of their distance from a scattering region at 110 pc. Both latitude (blue) and longitude (brown) data exhibit a logarithmic dependence, with the dashed lines indicating best-fit relations that show slightly varying constants for latitude and longitude.

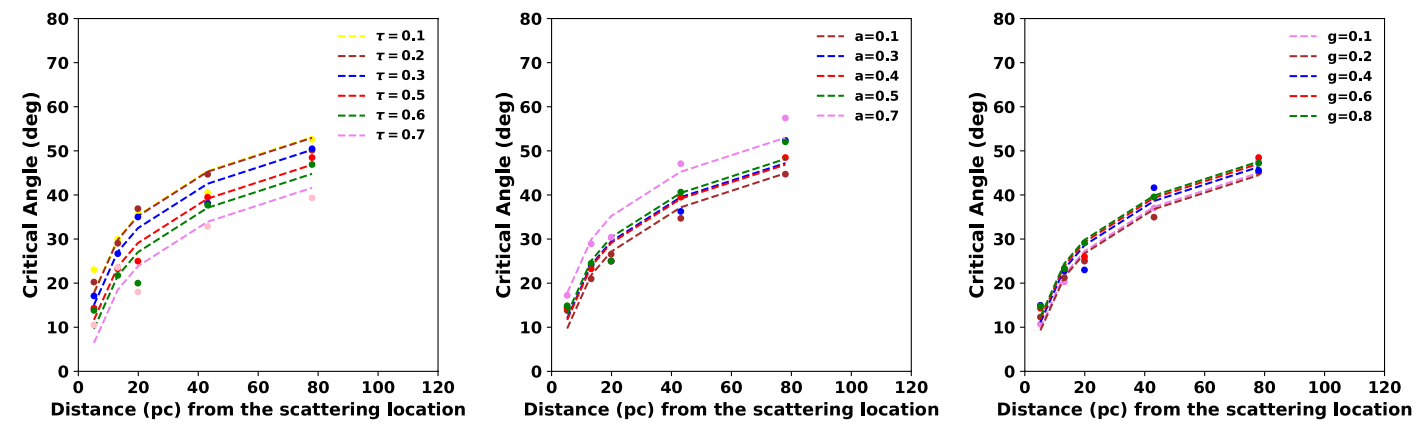
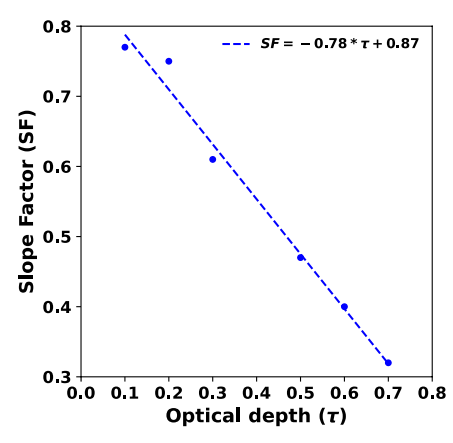


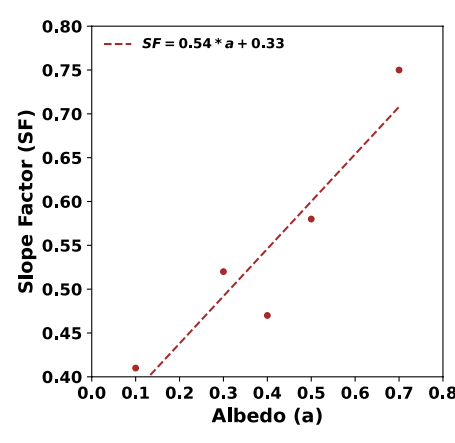
Figure 8. Variation of the critical angle (θ_c) with optical depth (τ) and optical parameters a and g. As τ increases, θ_c decreases, whereas higher values of a and g lead to an increase in θ_c .

Figure 10 compares the 1σ contour plots of the optical constants derived from the SS and SMS models with the 1σ and 2σ contours obtained from the MS model. It illustrates the degree to which varying values of SS, MS, and SMS fluxes align with the observed UV background as dust parameters (a and g) range from 0 to 1. Although the most probable parameters overlap within these contours, the unexpected intersection between MS and SMS at the 1σ boundary suggests that substituting single- for multiple-scattering in half the stars, to reduce computation, introduced discrepancies.

We also confirmed our SMS model using Voyager observations taken from Sujatha et al. (2005) toward the Ophiuchus region at 1100 Å. As we have developed our empirical model for lower optical depth, we limited our data

set to six observations from the Ophiuchus region. Although the majority of dust in the Ophiuchus region resides in the molecular cloud, Sujatha et al. (2005) discovered that scattering primarily occurs from the thin foreground cloud. After running the SS and SMS models with a step size of 0.01 for optical constants a and g, we calculated the optimal values for each observation using reduced chi-square analysis. The predictions of the MS model for the best-fit parameters obtained from the SMS model are compared with the SMS outputs and are plotted in Figure 12 along with the observed values. The strong correlation (89%) between SMS and MS models suggests the adaptation of the simulated model to the Monte-Carlo multiple scattering model. The predictions of each model for the best-fit parameters are shown in Table 4.





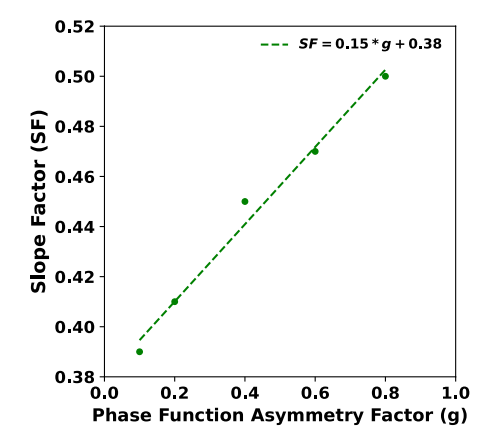


Figure 9. The linear dependence of the SF in θ_c (Equation (5)) on optical depth (τ) and optical constants (a and g) incorporated into the final expression (Equation (6)).

Details of FUV Radiation of GALEX Deep Observation Tile CDFS										
Tile Name	gl (deg)	gb (deg)	Optical Depth	Total Diffuse Emission	Foreground Emission	Background Emission (photons cm ⁻² s	SS Prediction (a = 0.6, g = 0.65) $^{-1} \text{ sr}^{-1} \text{ Å}^{-1})$	SMS Prediction $(a = 0.5, g = 0.7)$		
CDFS_01	223.93	-55.50	0.07	377	133	244	245	251		
CDFS_02	221.77	-54.31	0.08	455	164	291	275	289		
CDFS_03	222.89	-53.48	0.09	570	244	326	331	348		
CDFS_04	225.32	-54.80	0.08	441	203	238	269	279		
CDFS_05	222.32	-55.28	0.09	462	170	292	298	308		
CDFS_06	224.55	-53.81	0.08	504	145	359	293	306		
CDFS_07	225.70	-55.55	0.06	362	174	188	220	226		
CDFS_08	226.20	-54.70	0.08	418	167	251	282	292		
CDFS_09	225.74	-53.79	0.07	480	175	305	249	259		

92

302

Table 2
Details of FUV Radiation of GALEX Deep Observation Tile CDFS

6. Results and Discussions

0.08

394

-54.60

CDFS_10

222.68

This study compares and analyses dust-scattered starlight estimated through single-scattering and multiple-scattering models across the UV sky. We developed a simulated multiple-scattering model dependent on the critical angle (θ_c) , which is in turn influenced by optical depth (τ) , albedo (a), and phase function asymmetry factor (g). This model utilizes output from the single-scattering model to replace the complex multiple-scattering model. The primary conclusions are outlined below:

- (i) Modeling of dust-scattered starlight is primarily influenced by its intrinsic luminosity, spectral energy distribution, and the local geometry of stars and dust in any region.
- (ii) At higher optical depths, MS intensities reasonably align with the observed intensities due to the increased complexity of photon interactions.
- (iii) The scattering intensity of UV bright stars reaches its peak near the stellar disk and decreases rapidly to one-tenth of its maximum value within an angular separation of 10°-15°, ultimately blending with the background at approximately

40°-50°. Furthermore, stars that contribute minimally to scattering, owing to their lower luminosity or greater distance, necessitate a larger angular separation to achieve an equivalent one-tenth reduction in scattering intensity.

287

299

- (iv) The variation in single- and multiple-scattered intensity at any angular separation can be expressed mathematically as $I_{\theta} = I_0(1 \tanh(\text{SP} \times \theta))$, where I_0 and I_{θ} represent the scattered intensity measured at angular separations of 0.5 and θ from the line of sight, respectively.
- (v) The SP related to the scattering contribution of each star in relation to angular separation exhibits a declining pattern as stellar distance increases (Equation (3)).
- (vi) Depending on the relative position of the contributing star and dust, the MS intensities can increase up to 200% more than that of SS intensities due to additional scattering paths, overlapping angular distributions, increased effective albedo, and photon-trapping phenomena.
- (vii) Both single- and multiple-scattered intensities become identical at a critical angle, θ_c , which exhibits a logarithmic relationship with the stellar distance from the scattering location (Equations (4) and (5)).

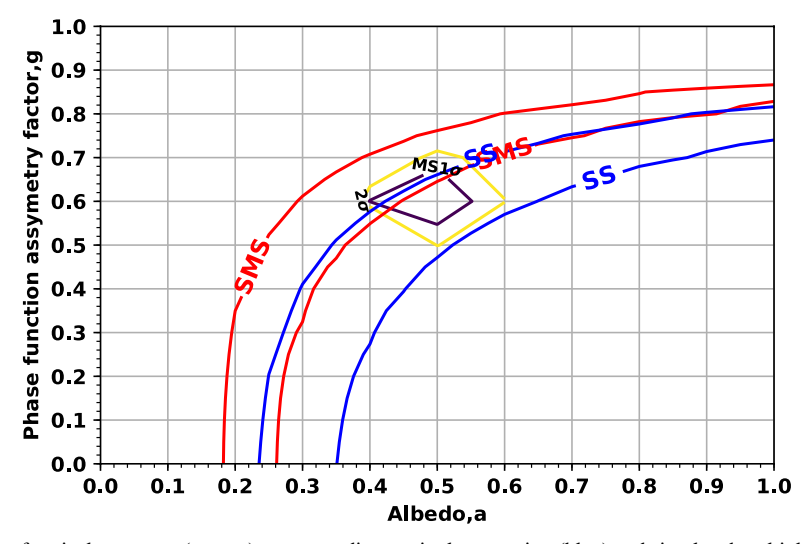


Figure 10. 1σ confidence contours of optical constants (g vs. a) corresponding to single-scattering (blue) and simulated multiple-scattering (red) model outputs are plotted here. 1σ and 2σ confidence contours of the multiple-scattering model outputs using the most contributing stars are also overplotted here.

 Table 3

 List of Most Contributing 24 Stars Toward CDFS Region

HIPNO	gl (deg)	gb (deg)	E(B-V)	Distance (pc)	Spectral Type	Stellar Flux at 1550 Å (erg cm ⁻² s ⁻¹ Å ⁻¹)
26727	206.45	-16.59	0.05	250.63	O9.5Ib	4.31E-08
39953	262.80	-7.69	0.14	257.73	WC8	8.27E-08
26311	205.21	-17.24	0.01	411.52	B0Ia	2.62E-08
25930	203.86	-17.74	0.07	280.90	O9.5II	2.89E-08
26241	209.52	-19.58	0.04	406.50	O9III	1.65E-08
24436	209.24	-25.25	0.06	236.97	B8Ia	1.03E-08
27366	214.51	-18.50	0.02	221.24	B0.5Iavar	1.56E-08
39429	255.98	-4.71	0.00	429.19	O5IAf	3.22E-08
9640	136.96	-18.56	1.49	108.81	B8V	1.77E-07
26207	195.05	-12.00	0.12	323.63	O	1.75E-08
30324	226.06	-14.27	0.00	153.14	B1II/III	1.62E-08
26549	206.82	-17.34	0.06	352.11	O9.5V	7.65E-09
18246	162.29	-16.69	0.45	301.21	B1Ib	1.90E-08
26221	209.01	-19.38	0.29	450.45	O6	4.99E-09
25281	204.87	-20.39	0.00	276.24	B1V	5.65E-09
33579	239.83	-11.33	0.00	132.10	B2II	1.74E-08
24845	214.83	-26.24	0.00	330.03	B0.5IV	2.82E-09
68702	311.77	1.25	0.00	161.03	B1III	5.72E-08
60718	300.13	-0.36	0.00	98.33	B0.5IV	7.22E-08
26235	209.05	-19.37	0.16	581.40	O9.5Vpe	3.27E-09
32759	242.36	-14.49	0.09	242.13	B1.5IVne	5.40E-09
18614	160.37	-13.11	0.27	543.48	O7.5Iab:	1.13E-08
23972	209.14	-26.69	0.02	537.63	B2IVn	1.82E-09
25923	210.44	-20.98	0.00	473.93	BOV	2.40E-09

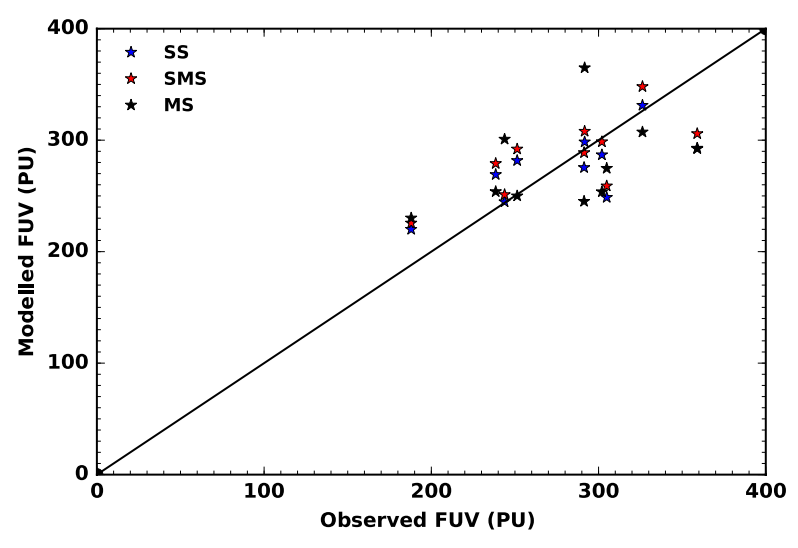


Figure 11. Correlation between observed diffuse FUV radiation and modeled outputs—SS (blue stars), MS (black stars), and SMS (red stars)—corresponding to the best-fit parameters in the CDFS region.

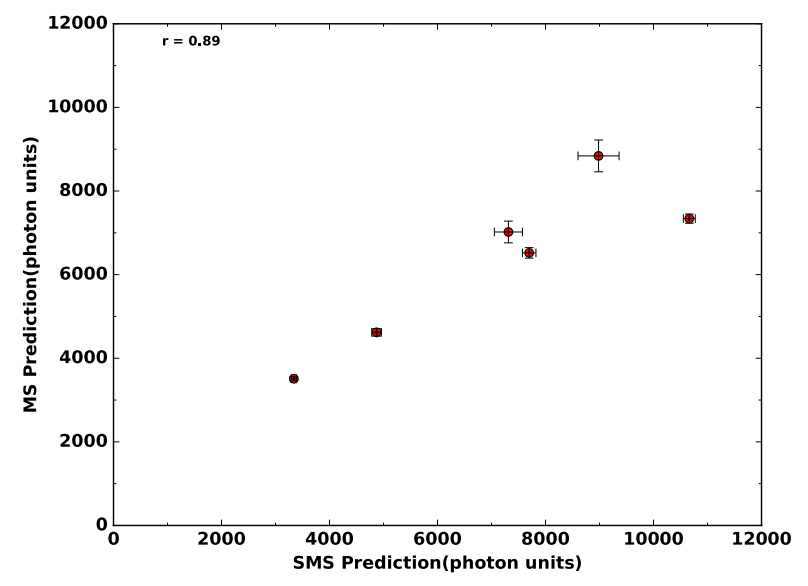


Figure 12. Correlation plot between simulated multiple-scattered (SMS) and MS predictions toward the Ophiuchus region.

 Table 4

 Details of Observed and Predicted Scattered Radiation in Ophiuchus Region

gl (deg) (gb	Observed Emission		SS Prediction		SMS Prediction			MS Prediction for the Best-fit Parameters of SMS			
	(deg)	Flux ^a	Error ^a	a	g	Flux ^a	a	g	Flux ^a	a	g	Flux ^a
355.5	31	3510	50	0.3	0.73	3516	0.2	0.68	3504	0.2	0.68	3340
355.5	30.3	4620	90	0.27	0.49	4621	0.21	0.47	4605	0.21	0.47	4871
357.5	27.5	6520	125	0.3	0.51	6519	0.21	0.61	6535	0.21	0.61	7698
356.4	29.2	7020	260	0.4	0.5	6958	0.29	0.52	7028	0.29	0.52	7313
358.1	25.2	7340	110	0.36	0.56	7341	0.25	0.5	7329	0.25	0.5	10,663
357	28.3	8840	380	0.5	0.75	8848	0.3	0.69	8844	0.3	0.69	8982

Note.

^a in photons cm⁻² s⁻¹ sr⁻¹ \mathring{A}^{-1} .

(viii) The critical angle of a star depends on the optical depth, τ , of the line of sight, optical constants: albedo, a, and phase function asymmetry factor, g, and is independent of longitude or latitude (Equation (7)).

7. Conclusion

This study compared the predictive power of our simulated multiple scattering model to the Monte Carlo Multiple Scattering model in the dust-rich interstellar medium. Both the Monte Carlo and simulated multiple scattering models offer pros and cons in accuracy, scalability, radiative transfer code inclusion, error characterization, generalizability, and hybrid modeling. Monte Carlo models are computationally expensive but accurate due to their stochastic, first-principles approach. Large-scale simulations and parameter sweeps are faster using empirical simulated multiple scattering models, which use simplified physics or regression. After Monte Carlo validation, these simulated techniques can be easily integrated into radiative transfer programs to reduce computing time and expand parameter exploration. Their accuracy is limited by training conditions, therefore their use must be carefully considered, especially in high-precision astrophysical studies.

Future research in complex scattering environments like dusty star-forming galaxies or high-redshift UV fields could benefit from hybrid modeling frameworks, which use Monte Carlo outputs to refine simulated predictions using machine learning. They scale better with spatial or angular resolution, enabling numerous scattering corrections in real-time astronomical data pipelines, remote sensing, and Earth observation. To validate the above relations across diverse regions in the sky, we will apply the concept to additional realistic instances in various sky locations and refine the model as needed, especially in dense regions. Our aim is to create a global model to estimate diffuse UV radiation at any sky location with improved accuracy.

Acknowledgments

This research is based on data from NASA's GALEX program. Data presented in this paper were obtained from the Mikulski Archive for Space Telescopes (MAST). STScI is operated by the Association of Universities for Research in Astronomy, Inc., under NASA contract NAS5-26555. S.N.V.

acknowledges the support of DST-FIST. Programming languages C, GDL and Python were used for the data analysis. We thank the anonymous referee for the valuable comments, which helped clarify several aspects of the paper.

Facility: GALEX.

Data Availability

The data that support the findings of this study are publicly available in GALEX-MAST archive at https://galex.stsci.edu/GR6/.

ORCID iDs

Nimmi Narayanan https://orcid.org/0000-0003-3447-7010 N. V. Sujatha https://orcid.org/0000-0001-6787-6080

References

```
Bernstein, R. A., Freedman, W. L., & Madore, B. F. 2002, ApJ, 571, 107
Bohlin, R. C., Savage, B. D., & Drake, J. F. 1978, ApJ, 224, 132
Corradi, W. J. B., Franco, G. A. P., & Knude, J. 2004, MNRAS, 347,
   1065
Draine, B. T. 2003, ARA&A, 41, 241
Gordon, K. D. 2004, in Astrophysics of Dust, ASP Conf. Ser., 309, ed.
   A. N. Witt, G. C. Clayton, & B. T. Draine (San Francisco, CA: ASP), 77
Henry, R. C. 1991, ARA&A, 29, 89
Henry, R. C., Murthy, J., Overduin, J., & Tyler, J. 2014, ApJ, 798, 14
Henyey, L. G., & Greenstein, J. L. 1941, ApJ, 93, 70
Kurucz, R. L. 1992, in The Stellar Populations of Galaxies, IAU Symp., 149,
  ed. B. Barbuy & A. Renzini (Dordrecht: Kluwer Academic Publishers), 225
Martin, D. C., Fanson, J., Schiminovich, D., et al. 2005, ApJ, 619, L1
Morrissey, P., Conrow, T., Barlow, T. A., et al. 2007, ApJS, 173, 682
Murthy, J. 2016, MNRAS, 459, 1710
Murthy, J., & Henry, R. C. 1995, ApJ, 448, 848
Murthy, J., Henry, R. C., & Sujatha, N. V. 2010, ApJ, 724, 1389
Narayanan, N., Menon, S. S., & Sujatha, N. V. 2023, AdSpR, 71, 1059
Perryman, M. A. C., Lindegren, L., Kovalevsky, J., et al. 1997, A&A,
   323, L49
Savage, B. D., & Mathis, J. S. 1979, ARA&A, 17, 73
Steinacker, J., Baes, M., & Gordon, K. 2013, ARA&A, 51, 63
Sujatha, N. V., Chakraborty, P., Murthy, J., & Henry, R. C. 2004, BASI,
   32, 151
Sujatha, N. V., Murthy, J., Karnataki, A., Henry, R. C., & Bianchi, L. 2009,
    \рJ, 692, 1333
Sujatha, N. V., Murthy, J., Shalima, P., & Henry, R. C. 2007, ApJ, 665, 363
Sujatha, N. V., Murthy, J., Suresh, R., Henry, R. C., & Bianchi, L. 2010, ApJ,
   723, 1549
Sujatha, N. V., Shalima, P., Murthy, J., & Henry, R. C. 2005, ApJ, 633, 257
Trumpler, R. J. 1930, PASP, 42, 214
Weingartner, J. C., & Draine, B. T. 2001, ApJ, 548, 296
```